Bio-Design and Manufacturing (2025) 8:742–758
https://doi.org/10.1631/bdm.2400375

RESEARCH ARTICLE

Reactive oxygen species scavenging hydrogel for wound healing in diabetic mice

Kaiyue Liu[1] · **Ruimei Jin**[1] · **Mengyu Yang**[1] · **Yachao Yu**[1] · **Jingmei Liu**[1] · **Chenghao Li**[1] · **Chen Zhang**[1] · **Hua Zhao**[1] · **Donghui Zhao**[2] · **Fangxia Guan**[1] · **Minghao Yao**[1]

Received: 14 September 2024 / Accepted: 1 April 2025 / Published online: 6 September 2025

Abstract

Excessive production of reactive oxygen species (ROS) and bacterial infection are intractable obstacles for wound healing in diabetic foot ulcers. Here, we devised a novel approach using a multifunctional hydrogel to achieve self-cascade glucose depletion and ROS scavenging, thereby modifying the diabetic wound microenvironment. In this study, using polyvinyl alcohol (PVA), borax, oligomeric proanthocyanidins (OPC), and nanozymes (AuPt@PDA), a PVA/Borax/OPC/AuPt@PDA (PBON) hydrogel was prepared by a one-step process. The PBON hydrogel combined with near-infrared (NIR) treatment can match the complicated and changeable microenvironment in the diabetic high-mobility region through glucose depletion, ROS scavenging, photothermal therapy (photothermal conversion 81.9%), and deformation adaptation, thus promoting wound healing close to the hip in diabetic mice through angiogenesis and epidermal regeneration by collagen deposition. This approach provides a simple, safe, and efficient treatment for diabetic wounds in mobile regions.

Graphical abstract

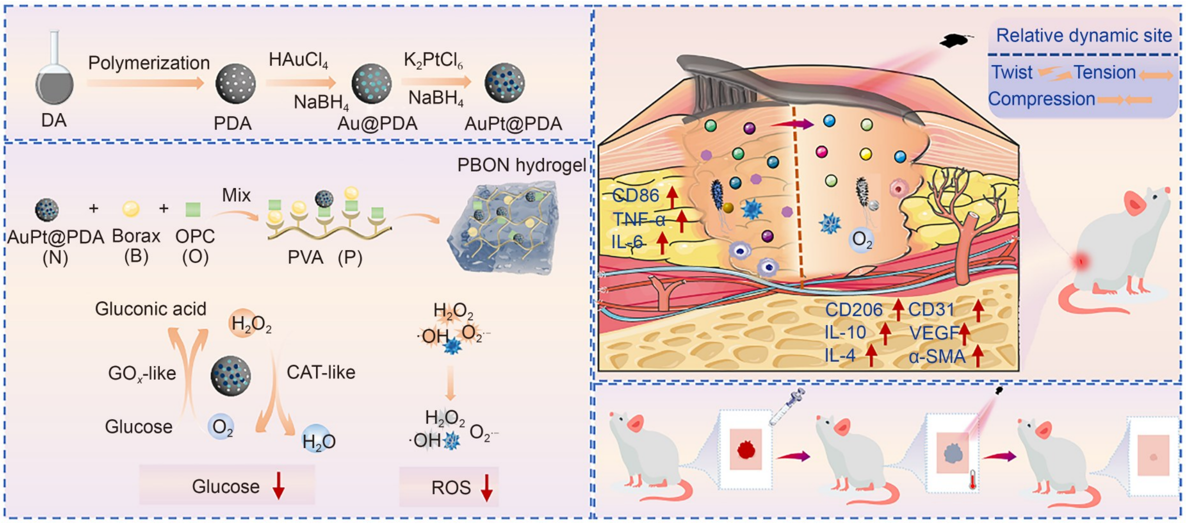

Keywords Diabetic wound · High-mobility region · Multifunctional hydrogel · Nanozymes · Photothermal antibacterial

---

Kaiyue Liu and Ruimei Jin have contributed equally to this work.

✉ Donghui Zhao
zhaodonghui1122@cczu.edu.cn

✉ Fangxia Guan
guanfangxia@126.com

✉ Minghao Yao
yao453343550@126.com

[1] School of Life Sciences, Zhengzhou University, Zhengzhou 450001, China

[2] School of Pharmacy & School of Biological and Food Engineering, Changzhou University, Changzhou 213164, China

1 Introduction

The number of diabetic patients worldwide is growing rapidly, and impaired wound healing and subsequent development of chronic wounds, such as diabetic foot ulcers (DFUs), are common and serious complications of diabetes [1]. Although treatments such as growth factor-based therapies and bioengineered skin for DFUs have been introduced into the clinic in the last few decades, their efficacy is limited and >50% of patients with DFUs do not respond to these treatments [2]. Hydrogels are effective materials used to treat diabetic wounds. However, conventional hydrogels are relatively monofunctional and cannot address the unique physiologic microenvironment of such wounds. In addition, treatment of wounds in special movement areas such as joints, axillae, and muscle folds remains challenging due to low adhesion, poor deformability, difficulty in fixation, and insufficient dressing coverage compared with wounds on flat parts of the body [3]. Thus, there is an urgent need for a multifunctional hydrogel to be able to regulate the diabetic microenvironment, decrease glucose, have antimicrobial properties, and be suitable for promoting diabetic wound healing in mobile regions.

The high glucose concentration in diabetic wounds leads to the secretion of large amounts of reactive oxygen species (ROS) [4]. Furthermore, the accumulation of inflammatory cytokines and the resulting oxidative stress can impair angiogenesis, which affects diabetic wound healing [5, 6]. An imbalance between endogenous antioxidants and ROS, including superoxide anions, hydroxyl radicals, singlet oxygen, and hydrogen peroxide, in the body is the main manifestation of oxidative stress [7]. Antioxidants can scavenge excess ROS and maintain the balance between endogenous antioxidants and ROS. Grape seed extract is rich in flavonoids, mainly oligomeric proanthocyanidins (OPC), and is widely used as an antioxidant and a chemical anticancer agent [8]. Therefore, OPC was selected as an antioxidant to address excessive ROS production.

Bacterial infection is another major risk factor associated with hyperglycemia [9]. Thus, wound dressings with antimicrobial properties are essential for diabetic wound healing [10]. Recently, photothermal therapy (PTT) has been used to effectively destroy bacteria and biofilms because of its efficient antimicrobial properties, good controllability, non-invasiveness, and prevention of multidrug-resistant bacteria [11, 12]. Many inorganic materials (e.g., gold nanoparticles (AuNPs), platinum nanoparticles (PtNPs), graphene, carbon nanotubes, and transition metal disulfides) have been reported to exhibit good PTT effects [13, 14]. In addition, AuNPs have glucose oxidase (GO$_x$) activity and low cytotoxicity [14–16]. PtNPs have catalase-like (CAT) activity and can convert H_2O_2 to O_2, which is beneficial for wound healing [17]. Therefore, AuPt bimetallic nanozymes not only have photothermal effects, but can also perform self-cascade glucose depletion and H_2O_2 scavenging.

Polyvinyl alcohol (PVA) is a biocompatible, polar polymer that readily forms cross-linked structures in solution through intramolecular or intermolecular hydrogen bonding or chemical bonding [18]. Borax, a cross-linking agent, in its hydrolyzed anionic form can form B–O bonds with two diols, creating borate bonds [19]. The –OH groups of PVA and Borax allow PVA-Borax hydrogels to bind to a wide range of substances via hydrogen bonding [20]. Polydopamine (PDA) acts as a good carrier [21], enabling slow release of metal ions at wound sites through chelation with metal ions, thereby avoiding biotoxicity [22].

Based on the above, a multifunctional nanocomposite hydrogel, PVA/Borax/OPC/AuPt@PDA (PBON) hydrogel, was prepared in this study (Scheme 1). Loading of AuPt@PDA nanozymes allows the development of hydrogels with GO$_x$-like, CAT-like activities, and PTT activity, targeting the specific microenvironment of diabetic wounds, namely hyperglycemia, elevated ROS levels, hypoxia, and infection susceptibility. Furthermore, the rapid gelation, injectability, tissue-adhesion, variability, self-healing, and antioxidant properties of PBON hydrogels make them particularly suitable for diabetic wounds in mobile regions. Finally, the wound-healing effect of the nanocomposite PBON hydrogel was evaluated in the mobile regions of diabetic mice.

2 Methods

2.1 Detection of GO$_x$-like and CAT-like activities of PBON hydrogels

The GO$_x$-like ability of hydrogels was tested using a glucometer. Briefly, N_1, N_2, N_3, and 100 μL of PBO, PBON$_1$, PBON$_2$, and PBON$_3$ hydrogels were coincubated with 16.7 mmol/L glucose solution (according to a volume ratio of 1:4 of nanozymes and glucose solution) [23], and the glucose concentration was measured every 12 h using a glucometer.

A portable dissolved oxygen meter (JPBJ-608, Shanghai Yidian Scientific Instrument Co., Ltd., China) was used to test the O_2 production capacity of AuPt@PDA and hydrogels. Briefly, N_1, N_2, N_3, and 100 μL of PBO, PBON$_1$, PBON$_2$, and PBON$_3$ hydrogels, separately, were incubated with 4 mL of 5 mmol/L H_2O_2 for 20 min at 1000 r/min and room temperature, and the O_2 produced by the different hydrogels was recorded by a portable dissolved O_2 meter. The control group was 5 mmol/L H_2O_2.

An H_2O_2 content assay was used to determine the H_2O_2 scavenging efficiency of the hydrogels. Briefly, N_1, N_2, N_3, and 100 μL of PBO, PBON$_1$, PBON$_2$, and PBON$_3$ hydrogels, separately, were incubated with 4 mL of 5 mmol/L H_2O_2 for 20 min at 1000 r/min and room temperature, and the residual H_2O_2 content of each group was quantified by measuring absorbance using an enzyme marker at 415 nm. The same control group was used as for the previous experiment. The

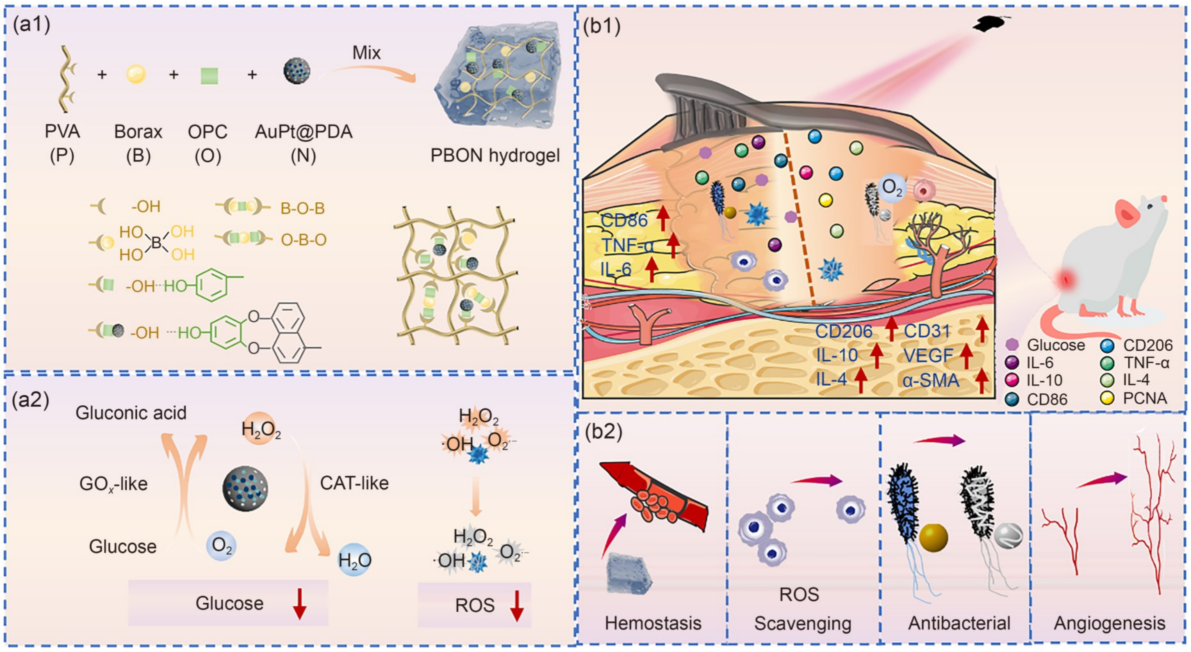

Scheme 1 AuPt@PDA nanozyme-loaded multifunctional hydrogels for promoting wound healing in mobile regions in diabetic mice. (a) Schematic of the synthesis process of multifunctional PBON hydrogel and PBON for self-cascading glucose depletion and ROS scavenging. (b) Rapidly prepared PBON hydrogel dressings using simple mixing to promote wound healing in diabetic wounds through hemostasis, hypoglycemia, inflammation reduction, bacteriostasis, and vascular regeneration

H_2O_2 scavenging capacity of the hydrogel was calculated according to the following equation:

$$r_{H_2O_2\text{-scavenging}} = (1-W_h/W_c)\times 100\%, \quad (1)$$

where W_h represents the absorbance of the hydrogel-treated group and W_c represents the absorbance of the control group.

2.2 Determination of the antioxidant properties of PBON hydrogels in vitro

The antioxidant properties of hydrogels were evaluated in vitro by 1,1-diphenyl-2-trinitrobenzenamine (DPPH) radical and hydroxyl radical scavenging, the specific steps of which are shown in the supplementary information. A superoxide dismutase (SOD) kit was used to test the scavenging capacity of the hydrogels for superoxide anions, as previously reported [24].

2,7-Dichlorodihydrofluorescein diacetate (DCFH-DA) labeling was used to detect ROS levels in H_2O_2-induced L929 cells. DCFH-DA was deacetylated to generate DCFH after entering the cells and oxidized by ROS to generate the highly fluorescent compound DCF, which was observed under fluorescence microscopy [25]. The detailed steps are shown in the supplementary information.

2.3 Biocompatibility of PBON hydrogels in vitro

The cytocompatibility of the hydrogels was assessed using a cell counting kit-8 (CCK-8) and live/dead fluorescence double staining. Mouse fibroblasts (L929) were used for this experiment [26].

The blood compatibility of the hydrogels was evaluated by measuring hemolysis. First, 50 μL samples of PBO, PBON$_1$, PBON$_2$, and PBON$_3$ hydrogels were prepared. The samples were placed at the bottom of a 1.5-mL centrifuge tube. Then, 1 mL of NaCl saline was added and incubated at 37 °C for 30 min. Then, 20 μL of blood was added, and the mixture was further incubated at 37 °C for 1 h. The samples were centrifuged at 2000 r/min for 5 min, and the absorbance of the supernatant was determined by an enzyme marker at 540 nm. The positive control was 0.1% TritonX-100. The negative control was Tris-HCl. The hemolysis rate was calculated by the following formula:

$$r_{\text{Hemolysis}} = (A_e - A_n)/(A_p - A_n)\times 100\%, \quad (2)$$

where A_e, A_p, and A_n represent the absorbance values of the experimental group, positive control group, and negative control group, respectively.

2.4 Detection of the photothermal properties and antimicrobial capacity of PBON hydrogels

A near-infrared laser (NIR, MDLIII-808 nm, 2.5 W) was used to detect the photothermal capacity of PBON hydrogels. PBO, PBON$_1$, PBON$_2$, and PBON$_3$ hydrogels were evaluated for bacteriostatic activity in vitro using *Escherichia coli* (*E. coli*, Gram-negative) and *Staphylococcus* *aureus* (*S. aureus*, Gram-positive). Detailed steps are shown in the supplementary information.

2.5 Detection of biocompatibility and hemostatic properties of $PBON_2$ hydrogel in vivo

To establish the hydrogel subcutaneous embedding model, briefly, 100 μL of $PBON_2$ hydrogel was transplanted subcutaneously into mice after anesthesia; mice were routinely fed for 7 d after surgery. The skin and major organs (heart, liver, spleen, lungs, and kidneys) were extracted and stained with hematoxylin-eosin (H&E). In addition, the potential side effects of $PBON_2$ hydrogel on the liver were evaluated by histological and blood biochemical tests (aspartate aminotransferase (AST), alanine transaminase (ALT), and alkaline phosphatase (AKP)). Healthy mice without hydrogel transplantation were used as controls.

The coagulation ability of the hydrogels in vitro was evaluated based on the blood coagulation index (BCI). The hemostatic properties of $PBON_2$ hydrogel were tested using femoral artery hemorrhage, acute hepatic hemorrhage, and tail hemorrhage models [27, 28]. Detailed procedures are displayed in the supplementary information.

2.6 Establishment and treatment of the *S. aureus*-infected diabetic mouse wound model

Detailed steps are presented in the supplementary information. A camera recorded the wound area on Days 0, 3, 7, 14, and 21, and the wound area was measured using image analysis software (ImageJ). The wound healing rate was calculated using the following formula:

$$r_{\text{Wound-healing}} = (S_0 - S_\text{n})/S_0 \times 100\%, \quad (3)$$

where S_0 and S_n represent the initial wound area and the healed wound area, respectively.

2.7 Infection assessment, bacteriostatic evaluation, ROS quantification in vivo, and H&E and Masson staining at wounds

Detailed steps are presented in the supplementary information.

2.8 Immunofluorescence

To evaluate wound tissue regeneration, we used immunofluorescence to detect the expression of inflammatory factors (interleukin-6, IL-6; interleukin-10, IL-10; lymphocyte activation antigen, CD86; macrophage surface receptor, CD206; tumor necrosis factor-α, TNF-α; interleukin-4, IL-4) as well as angiogenesis (platelet endothelial cell adhesion molecule, CD31; vascular endothelial growth factor, VEGF; α-smooth muscle actin, α-SMA) and cell proliferation (proliferating cell nuclear antigen, PCNA) in wounds.

2.9 Statistical analysis

Graphing was performed using GraphPad Prism, and all results were analyzed using *t*-test or one-way analysis of variance (ANOVA). All data are expressed as mean±standard deviation from at least three independent experiments, with $^{*}p<0.05$, $^{**}p<0.01$, $^{***}p<0.001$, and $^{****}p<0.0001$ indicating statistically significant results.

3 Results and discussion

3.1 Characterization of AuPt@PDA NPs as well as scanning electron microscopy (SEM) and energy dispersive X-ray spectroscopy (EDS) analysis of PBON hydrogels

PDA NPs were synthesized as previously reported [29]. The synthesis flow diagram of AuPt@PDA is shown in Fig. S1 (supplementary information). Dynamic light scattering and zeta potential measurements showed that PDA NPs had an average diameter of 323 nm and a zeta potential of −21.83 mV (Figs. S2a and S2b in the supplementary information) while AuPt@PDA NPs displayed an average diameter of 263 nm and a zeta potential of −17.7 mV. In addition, dynamic light scattering measurements demonstrated that AuPt@PDA NPs remained stable for 7 d with negligible changes in size and polydispersity index (PDI) (Fig. S2c in the supplementary information). Next, the elemental composition of AuPt@PDA NPs was detected by X-ray photoelectron spectroscopy (XPS) (Fig. S2d in the supplementary information). The XPS spectra showed peaks corresponding to C 1s, N 1s, O 1s, Au 4f, and Pt 4f, which indicated that both AuNPs and PtNPs were successfully synthesized and deposited in PDA NPs. Further, the transmission electron microscopy (TEM) results showed that both PDA NPs and AuPt@PDA NPs were uniformly spherical and showed little changes in size (Fig. 1a).

To investigate the effect of the nanozymes on the hydrogel, four hydrogel formulations were prepared, and their compositions are shown in Fig. S3 (supplementary information). In PBO and PBON hydrogels, the final PVA concentration was 3%, the Borax concentration was 0.5%, and the OPC concentration was 1%. The concentrations of AuPt@PDA in $PBON_1$, $PBON_2$, and $PBON_3$ hydrogels were 0.5, 1.0, and 2.0 mg/mL, respectively. To facilitate visual observation, the gelation process of the PBO and $PBON_2$ hydrogels is shown. After mixing, a hydrogel was formed in situ, adhering tightly to the bottom of the bottle without flow (Fig. 1b), indicating the formation of PBO and PBON hydrogels.

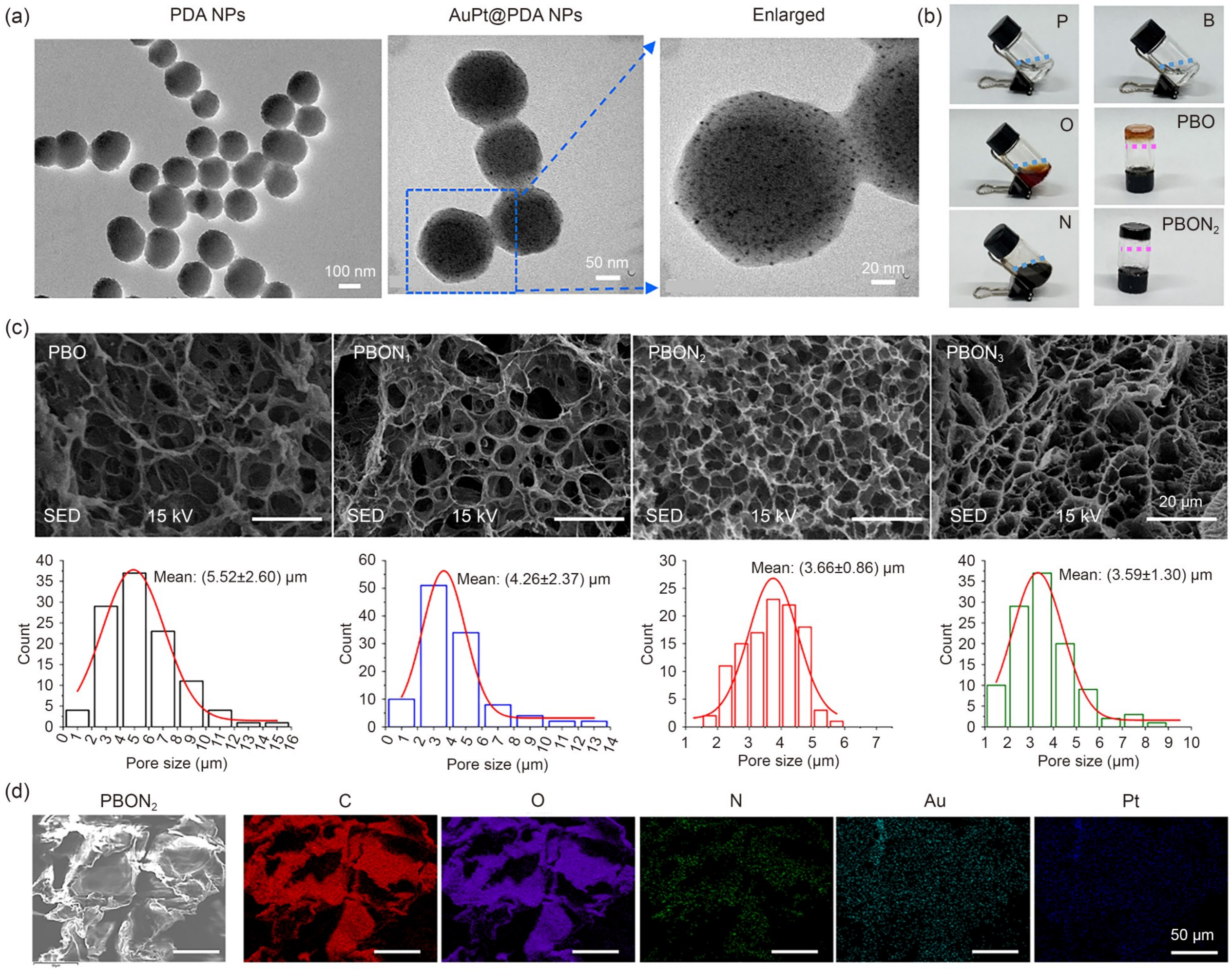

Fig. 1 Characterization of AuPt@PDA NPs, and SEM and EDS of PBON hydrogels. (a) TEM images of PDA NPs and AuPt@PDA NPs. (b) Photographs of PBO and $PBON_2$ hydrogels (P for PVA, B for Borax, O for OPC, and N for AuPt@PDA NPs). (c) SEM images of hydrogels and pore size distribution. (d) EDS images of the $PBON_2$ hydrogel

Hydrogels have a three-dimensional (3D) structure similar to that of the extracellular matrix (ECM), and are favorable for maintaining the activity of biomolecules and cells [30]. Therefore, the micromorphology of the lyophilized PBO and PBON hydrogels was observed using SEM; all had a porous network structure. SEM images showed a pore size distribution of 2–8 μm (Fig. 1c). The swelling equilibrium test showed that the PBON hydrogel exhibited a considerable swelling ratio at swelling equilibrium, >300% at 1 h in all groups (Fig. S4a in the supplementary information), indicating that the PBON hydrogel could absorb the excess fluid in the wound and maintain a moist environment during early stages of wound healing. Meanwhile, both PBO and PBON hydrogels exhibited similar and positive degradation properties. They lost nearly 43% and 29% of their original mass within the first five days, respectively (Fig. S4b in the supplementary information), indicating that their structural integrity was largely preserved. This preservation is critical to the protection of wounds during the inflammatory phase and the early stages of tissue formation [31]. In addition, elemental mapping was used to analyze the distribution of AuPt@PDA nanozymes inside the $PBON_2$ hydrogel. C, O, N, Au, and Pt were uniformly present (Fig. 1d), demonstrating that AuPt@PDA nanozymes were well-distributed in the PBON hydrogel.

3.2 Properties of PBON hydrogels: tissue-adhesion, deformability, self-healing, injectability, removability, and easy peeling

Good tissue-adhesion and deformability are particularly important for wound dressings targeting wounds in high mobility regions [32, 33]. The tissue-adhesion ability of PBON hydrogels was evaluated in the standardized porcine skin lap shear test (Fig. 2a). The tissue-adhesion strength of $PBON_1$, $PBON_2$, and $PBON_3$ hydrogels increased by 8.22 to 19.2 kPa compared to the PBO hydrogel (Fig. 2b). Among them, the adhesion strength of $PBON_2$ hydrogel to porcine

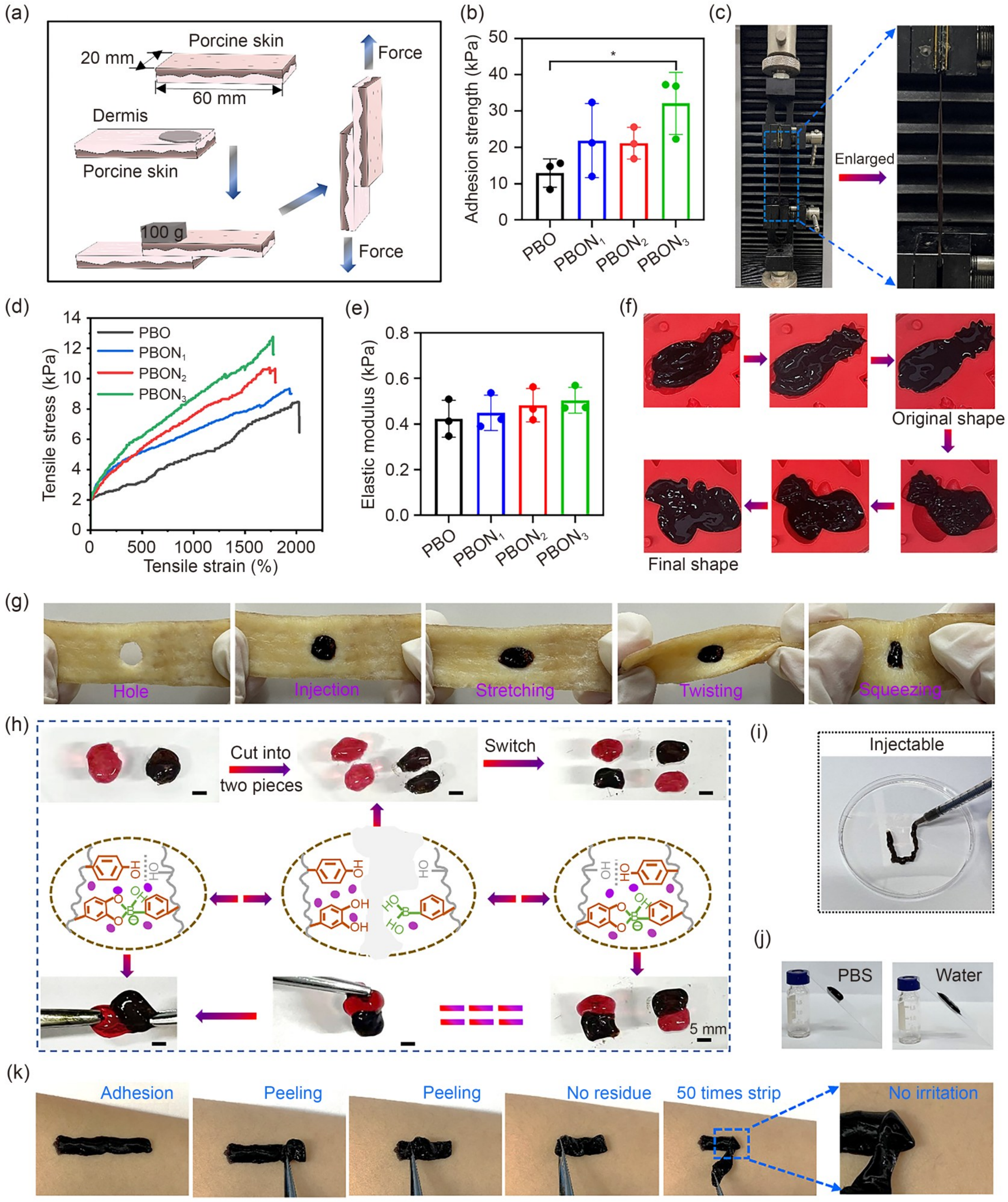

Fig. 2 Tissue-adhesion, tensile and shape-adaptive behavior, self-healing, injectability, removable behavior, and easy peeling of PBON hydrogels. (a) Schematic diagram of the lap shear test. (b) Adhesion strength of the hydrogel to porcine skin. (c) Photographs of the tensile properties of $PBON_2$ hydrogel. (d) Tensile stress–strain curves of PBON hydrogels with different AuPt@PDA contents. (e) Elastic modulus of PBON hydrogels with different AuPt@PDA contents. (f) Shape-adaptive behavior of $PBON_2$ hydrogel to static molds. (g) Shape-adaptive behavior of $PBON_2$ hydrogel to dynamic porcine skin wound. (h) Self-healing behavior of PBO and $PBON_2$ hydrogels. (i) Injectability of $PBON_2$ hydrogel. (j) Removability of the $PBON_2$ hydrogel. (k) Easy peeling of $PBON_2$ hydrogel. Data are expressed as mean±standard deviation (n=3); $^{*}P$<0.05

skin was 21.17 kPa, higher than that of commercial dressings (approximately 5 kPa), and was an effective value for adherence to diabetic wounds with skin laxity [34, 35]. The tissue-adhesion mechanism of hydrogels can be attributed to the high binding force of the catechol groups in PDA and OPC to the nucleophilic groups, including sulfhydryl groups, amines, and imidazole, in the peptides and proteins in the tissue.

We also measured the tensile ability of the hydrogel. The tensile ability of PBO, $PBON_1$, $PBON_2$, and $PBON_3$ hydrogels was 2023%, 1931%, 1794%, and 1741% (Figs. 2c and 2d), respectively, superior to those of most hydrogel wound dressings (usually <100%) [3]. In addition, compared with the PBO hydrogel, the cross-linking network structure enhanced the tensile stress of the PBON hydrogels from 8.47 to 12.77 kPa and the elastic modulus from 0.42 to 0.50 kPa

(Figs. 2d and 2e). Consequently, these results facilitate moving parts and serve as a strong guarantee of effective wound adhesion.

Further, static and dynamic methods were used to evaluate the shape-adaptive ability of the hydrogels. When the $PBON_2$ hydrogel fully adapted to the pineapple-shaped mold (original), it was transferred to a strawberry-shaped mold (final) and was still able to completely fill it (Fig. 2f). In addition, the $PBON_2$ hydrogel adapted firmly to porcine skin tissues and remained settled even after stretching, twisting, and squeezing (Fig. 2g), demonstrating the high adhesive strength between the skin tissue and the $PBON_2$ hydrogel. Thus, $PBON_2$ hydrogel has the potential to establish a stable and close contact between mobile regions and the wound surface.

Hydrogel breakup may lead to infection and loss of protective function. However, the dual dynamic bonding (boron ester bond and hydrogen bond) of the $PBON_2$ hydrogel provides excellent self-healing ability and avoids this risk (Fig. 2h). Further, the $PBON_2$ hydrogel can be molded into a "U" form, suggesting its good injectability (Fig. 2i). This property is critical for biomedical applications of hydrogels at irregular wound sites.

In addition, good removability ensures that the hydrogel dressing does not cause secondary damage to the wound during removal. The hydrogel in the control group remained intact after spraying with PBS (Fig. 2j), while the $PBON_2$ hydrogel sprayed with deionized water liquefied quickly and could be easily removed. In addition, the $PBON_2$ hydrogel allowed for easy peeling (Fig. 2k), and after 50 times repeated hydrogel adhesion to the skin (the author's arm), it could still be easily removed without any residue or skin irritation.

3.3 GO_x-like and CAT-like activities of the PBON hydrogels

GO_x-like and CAT-like activities of the PBON hydrogels formed a glucose-activated two-step cascade reaction. The Au group in AuPt@PDA nanozymes catalyzes glucose oxidation to produce gluconic acid and H_2O_2 [36, 37], completing the first step of the cascade reaction. Subsequently, the change in glucose content was determined. All three nanozyme groups (N_1, N_2, and N_3) resulted in a decrease in the glucose solution concentration and a more rapid decrease with increasing content of AuPt@PDA (Fig. S5 in the supplementary information). Of these, N_2 decreased from 16.7 to 3.7 mmol/L. Similarly, in PBO, $PBON_1$, $PBON_2$, and $PBON_3$ hydrogels, the glucose concentration decreased sequentially (Fig. 3a). Thus, AuPt@PDA and PBON hydrogels have GO_x-like activities that can promote glucose oxidation and increase the activity of the cascade reaction.

In chronic wounds, prolonged hypoxia prevents the generation of effective antioxidants, which leads to the production of excess ROS and a persistent inflammatory state [38, 39]. The Pt in AuPt@PDA nanozymes catalyzes the production of O_2 and H_2O from H_2O_2 [40], completing the second step of the cascade reaction, in which the change in O_2 production and H_2O_2 scavenging was detected. N_1, N_2, and N_3 produced O_2 faster with increasing AuPt@PDA content (Fig. 3b). Similarly, in PBO, $PBON_1$, $PBON_2$, and $PBON_3$ hydrogels, O_2 production increased sequentially to 9.22, 12.94, 15.15, and 21.93 mg/L, respectively. In addition, the scavenging rates of H_2O_2 by PBO, $PBON_1$, $PBON_2$, and $PBON_3$ hydrogels were 5.38%, 14.70%, 26.44%, and 48.63%, respectively (Fig. 3d). These results indicate that AuPt@PDA and PBON hydrogels have CAT-like activity to produce O_2 from H_2O_2, and that the O_2 concentration is concentration- and time-dependent. The properties of the $PBON_2$ hydrogel enable it to consume glucose effectively in the hypoxic, high-glucose microenvironment of DFUs.

3.4 Antioxidant activity of PBON hydrogels in vitro

Antioxidants can compensate for ROS overproduction and prevent the adverse effects of these free radicals [41]. In the antioxidant assay, DPPH has been widely used to assess the free radical scavenging efficiency of a variety of antioxidant substances. Antioxidants convert DPPH radicals into the corresponding colorless hydrazine (DPPH-H), and their ability to scavenge DPPH radicals is quantified by absorbance at 517 nm [42]. The color obviously changed from dark purple to light yellow with increased AuPt@PDA concentration after the addition of the PBON hydrogel (Fig. 3e), indicating that the hydrogel reacted with DPPH to form DPPH-H. The DPPH radical scavenging rates of PBO, $PBON_1$, $PBON_2$, and $PBON_3$ hydrogels reached 46.07%, 34.27%, 31.18%, and 26.12%, respectively. The scavenging activity of PBON hydrogels against hydroxyl radicals was determined by the Fenton reaction. The hydroxyl radical scavenging ratios of the PBO, $PBON_1$, $PBON_2$, and $PBON_3$ hydrogels were 46.42%, 43.84%, 27.17%, and 19.59%, respectively (Fig. 3f). With increasing nanozyme content, the hydroxyl radical scavenging ability of the hydrogel decreased. This may be due to the interaction between the nanozyme and OPC, which weakens the ability of the hydrogel to scavenge free radicals. In addition, the SOD activities of PBO, $PBON_1$, $PBON_2$, and $PBON_3$ hydrogels were 31.22, 28.33, 15.00, and 4.77 U/mL, respectively (Fig. 3g). These results indicate that PBON hydrogels have good free radical scavenging ability.

We further evaluated whether the antioxidant capability of PBON hydrogels could rescue intracellular ROS levels. High intracellular ROS levels were detected in cells treated with 500 μmol/L H_2O_2 (Fig. 3h). In contrast, the fluorescence intensity of cells treated with PBO and $PBON_2$ hydrogel was significantly lower than that of the H_2O_2 group

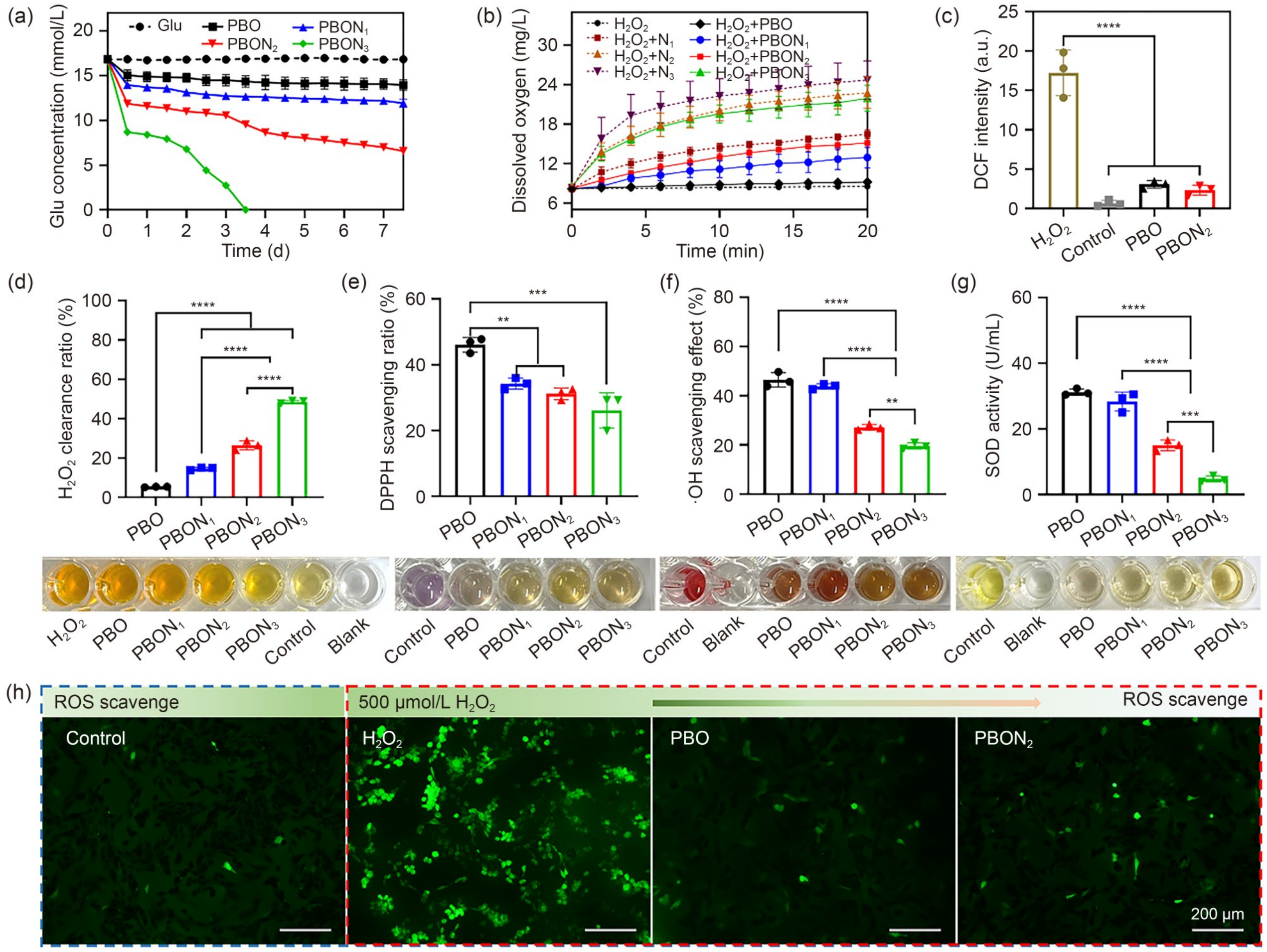

Fig. 3 GO_x-like, CAT-like activities and antioxidant capacity of PBON hydrogels. (a) GO_x-like activity of the hydrogels. (b) O_2 production of PBON hydrogels. (c) DCF fluorescence intensity. (d) Scavenging rate of H_2O_2 by hydrogels. (e) Scavenging rate of DPPH radicals by hydrogels. (f) Scavenging rate of hydroxyl radical by the hydrogels. (g) SOD activity of the hydrogels. (h) DCF fluorescence staining images of L929 cells after treatment with fresh medium (Control group), 500 μmol/L H_2O_2 (H_2O_2 group), 500 μmol/L H_2O_2+20 μL PBO hydrogel (PBO group), and 500 μmol/L H_2O_2+20 μL PBON$_2$ hydrogel (PBON$_2$ group). Data are expressed as mean±standard deviation (n=3); $^{**}p<0.01$, $^{***}p<0.001$, $^{****}p<0.0001$

(Fig. 3c), indicating that the PBON hydrogel has antioxidant capacity, protecting cells from damage by oxidative stress.

3.5 Biocompatibility of PBON hydrogels in vitro

The biocompatibility of PBON hydrogels was evaluated by CCK-8 and live/dead fluorescence double staining. A schematic representation of L929 cells cocultured with the hydrogel extract is shown in Fig. S6a (supplementary information). After coculture for 1 and 2 d, the cell viability of PBO, PBON$_1$, PBON$_2$, and PBON$_3$ hydrogels was >80% (Fig. S6b in the supplementary information), meeting the 70% international standard for biomaterials (ISO10993: 2009) [43]. The results of live/dead fluorescent staining of L929 cells were consistent with those of the cell viability assay (Fig. S6c in the supplementary information). Therefore, the PBON hydrogel has good cytocompatibility.

Next, the hemocompatibility of the PBON hydrogel was evaluated. After incubating the PBON hydrogel with blood for 1 h, the hemolysis rates of all hydrogels were below the international standard of 5% (Fig. S6d in the supplementary information) [44], which suggests that the PBON hydrogel has good hemocompatibility, being a very promising candidate for wound dressing. The morphology of the red blood cells (RBCs) was shown; the RBCs in each hydrogel group were clear and intact (Fig. S6e in the supplementary information).

3.6 Photothermal properties and antimicrobial activity of PBON hydrogels

Photothermal ablation can kill bacteria by utilizing the heat generated by photothermal agents under NIR irradiation (700–1400 nm), a safe and efficient strategy to prevent infection [45]. AuNPs have attracted extensive research interest due to their excellent photothermal effect, while PtNPs have been recently used due to their highly tunable scattering and radiation absorption [46, 47]. To evaluate the photothermal performance of PBON hydrogels, the temperature profiles of the hydrogels were measured under 808-nm laser irradiation. The temperature of a PBO hydrogel without AuPt@PDA remained constant after 300 s of NIR irradiation (0.3 W/cm^2, 808 nm). With an increased AuPt@PDA content, the temperature of the PBON hydrogel gradually increased from 24.3 to 50.4 °C (Figs. 4a1 and 4a2), indicating that the photothermal effect of the PBON hydrogel was dependent on the AuPt@PDA concentration. In addition, the temperature of PBON$_2$ gradually increased from 36.8 to 50.5 °C and further 63.6 °C when the NIR light intensity increased from 0.2 to 0.3 W/cm^2 and further 0.4 W/cm^2 (Fig. 4b). These results indicate that the prepared PBON$_2$ hydrogel can effectively convert NIR light energy into heat, having a tunable photothermal capability. After four photo-switching cycles, the rise and fall curves did not change significantly (Fig. 4c), reflecting the good photothermal stability of the PBON$_2$ hydrogel. The photothermal conversion efficiency (η) of the PBON$_2$ hydrogel was 81.9% (Fig. S7 in the supplementary information), suggesting that it could be an effective PTT agent and a candidate for PTT [23, 48]. In addition, its stronger photothermal properties allow PBON$_2$ to reach the desired photothermal inhibition temperature at 0.3 W/cm^2 (808 nm), which is lower than the maximum allowable limit of skin exposure to NIR light with an optical density of 0.33 W/cm^2 (808 nm), without the risk of thermal damage to surrounding tissues [14]. The controllable photothermal effect, good photothermal stability, and superior photothermal conversion efficiency support the use of PBON hydrogels as dressings in vivo with anti-infective and wound healing properties.

Bacterial infections can impede skin wound healing [49]. At a temperature >45 °C, proteins and enzymes in bacteria undergo denaturation, resulting in bacterial death [45]. *E. coli* (a Gram-negative bacterium) and *S. aureus* (a Gram-positive bacterium) are typical of the flora isolated from infected wounds [50, 51]. The photothermal antimicrobial properties of PBON$_2$ hydrogels against *E. coli* and *S. aureus* were evaluated to determine whether the heat generated by PBON$_2$ hydrogels under NIR irradiation could effectively eliminate bacteria. Compared with controls, the number of bacterial colonies in the PBON$_2$ hydrogel group treated with PTT for 10 min was significantly reduced, indicating a strong

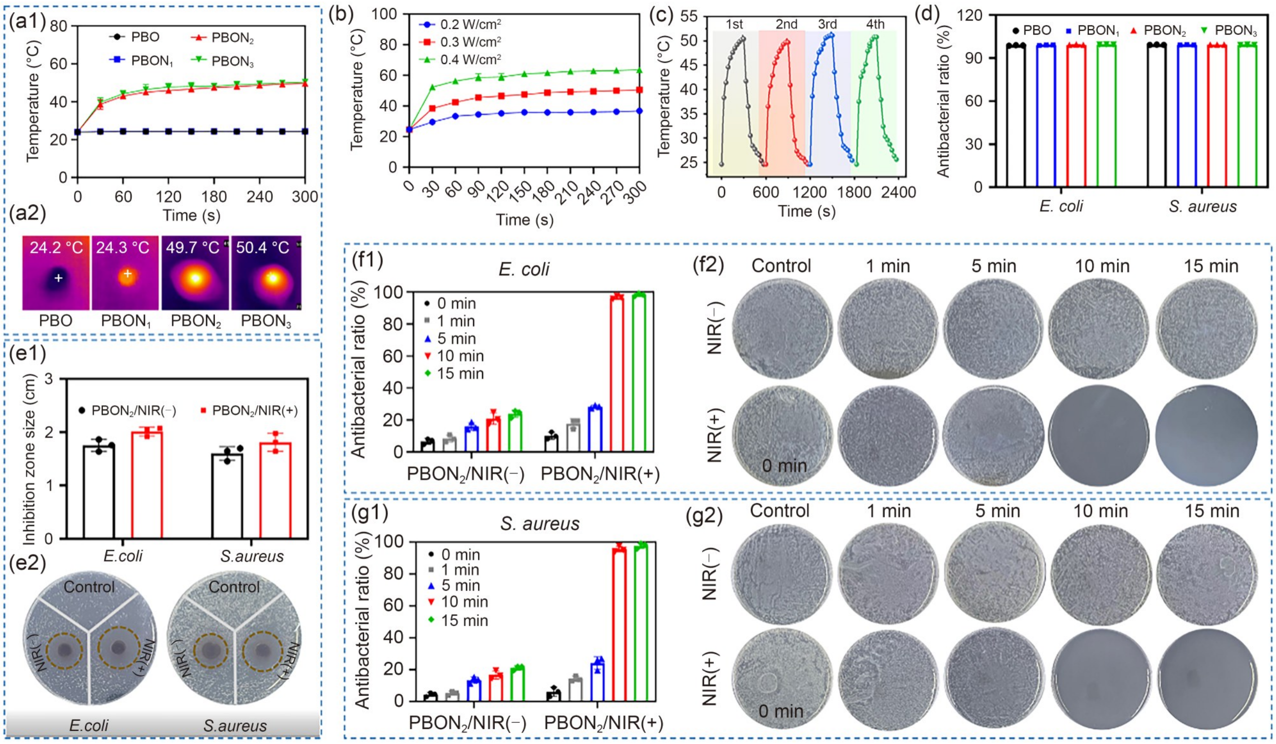

Fig. 4 NIR-assisted photothermal effect and bacteriostatic properties of PBON$_2$ hydrogels. (a) Temperature change curves within 300 s and real-time thermograms at 300 s for NIR-irradiated PBO, PBON$_1$, PBON$_2$, and PBON$_3$ hydrogels (808 nm, 0.3 W/cm^2). (b) Temperature change curves of the PBON$_2$ hydrogels irradiated by different NIR power levels (808 nm, 0.2 W/cm^2, 0.3 W/cm^2, 0.4 W/cm^2) for 300 s. (c) Temperature change curves of four "heating–cooling" cycles of NIR-irradiated PBON$_2$ hydrogel (808 nm, 0.3 W/cm^2). (d) Inherent inhibitory activities of PBO, PBON$_1$, PBON$_2$, and PBON$_3$ hydrogels. (e) Inhibition zone of PBON$_2$ hydrogel. Antibacterial ratio of *E. coli* (f1) and *S. aureus* (g1), and photographs of colonies on agar plates after NIR irradiation of PBON$_2$ hydrogels for 0, 1, 5, 10, and 15 min (f2, g2). Data are expressed as mean±standard deviation (n=3)

bactericidal effect. With longer irradiation time, the antibacterial effect showed a significant upward trend (Figs. 4f1 and 4g1). For an NIR laser irradiation time >10 min, almost all bacteria in the $PBON_2$ hydrogel group died (Figs. 4f2 and 4g2). In contrast, the $PBON_2$ hydrogel group without PTT showed almost no increase in the bacterial killing rate, indicating that the $PBON_2$ hydrogel alone could not significantly eliminate bacteria in a short period of time.

After coculturing bacteria with the hydrogels for 4 h without NIR, the PBO, $PBON_1$, $PBON_2$, and $PBON_3$ hydrogels removed 98.76% (99.26%), 99.03% (99.21%), 99.27% (99.31%), and 99.4% (99.21%) *E. coli* (*S. aureus*), respectively (Fig. 4d). Because of the strong antibacterial activity of OPC and AuPt@PDA, the antibacterial rate of the hydrogel was close to 100% [52, 53]. These findings indicate that the $PBON_2$ hydrogel can result in very good intrinsic bacterial inhibition and can be used as a long-term strategy to prevent or treat bacterial infections after rapid PTT bacterial inhibition.

Afterward, the antimicrobial activity of $PBON_2$ gels was evaluated using the universal plate diffusion method. The zones of inhibition for *E. coli* and *S. aureus* in the $PBON_2$/NIR(−) group were 1.75 and 1.60 cm, respectively, whereas those in the $PBON_2$/NIR(+) group were 2.01 and 1.81 cm, respectively (Figs. 4e1 and 4e2). These results indicate that the NIR-treated $PBON_2$ hydrogel had better antimicrobial activity.

3.7 Biocompatibility and hemostatic property of $PBON_2$ hydrogels in vivo

Based on its photothermal properties, enzyme-like activity, and antioxidant properties, the $PBON_2$ hydrogel was selected for animal experiments. The $PBON_2$ hydrogel was subcutaneously embedded into Kunming mice (KM) and its biosafety was evaluated by H&E staining and blood biochemical assays. H&E staining showed no obvious pathological changes and systemic damage to major organs (heart, liver, spleen, lung, kidney) and skin in mice in the $PBON_2$ hydrogel group compared with normal mice (Fig. 5a). Compared with normal mice, hydrogel treatment did not significantly change AST, ALT, and AKP levels in mice (Fig. S8 in the supplementary information). These data are consistent with the H&E staining results, indicating that the $PBON_2$ hydrogel did not cause systemic toxicity during treatment and had good biocompatibility in vivo, allowing it to be used as a wound dressing.

The procoagulant ability of the hydrogels was assessed by a whole blood coagulation assay. The lower the BCI, the faster the coagulation rate [54]. The BCI of the PBO, $PBON_1$, $PBON_2$, and $PBON_3$ hydrogels was 11.76%, 10.45%, 9.14%, and 6.24%, respectively, while that in the control and gauze groups was 99.13% and 52.39%, and these values were significantly higher than those of the hydrogel-treated groups ($p<0.0001$; Fig. S9a in the supplementary information). In contrast, the supernatants of the control and gauze groups were reddish (Fig. S9b in the supplementary information), whereas those of all hydrogel-treated blood samples were lighter, indicating that most blood treated with the PBON hydrogels had coagulated. Based on the above, the PBON hydrogel has a strong coagulation function.

The hemostatic ability of the $PBON_2$ hydrogel on complex wounds was tested on the femoral artery, acute liver, and acute tail hemorrhage models (Fig. 5b). After treatment with the $PBON_2$ hydrogel, the femoral artery, acute liver, and acute tail hemorrhages were controlled within 56, 38, and 29 s, respectively (Fig. 5c), compared to the untreated and gauze groups, which still showed significant hemorrhage after 106 s. Additionally, the blood loss of the femoral artery, acute hepatic, and acute tail hemorrhage models where the $PBON_2$ hydrogel was applied was 65.60, 43.13, and 39.77 mg, respectively, whereas the gauze group (the untreated group) reached 146.90 mg (284.43 mg), 113.53 mg (229.17 mg), 105.10 mg (262.83 mg), respectively (Fig. 5d). Overall, the $PBON_2$ hydrogel exhibited a significant hemostatic effect compared with the control ($p<0.0001$) and gauze ($p<0.01$) groups, which further demonstrates the good hemostatic potential of this hydrogel.

The hemostatic mechanism of hydrogels can be summarized into two aspects: (1) catechol groups in PDA and OPC can provide the hydrogel with good tissue adhesion, which enables the hydrogel to attach to the wound and provide a stable gel network that acts as a physical barrier to accelerate hemostasis [3, 55]; (2) multiple interactions, such as π-π stacking and hydrogen bonding, also contribute to adhesion, thereby inhibiting bleeding [34].

3.8 Establishment and treatment of the diabetic wound model

Next, the pro-healing effect of the $PBON_2$ hydrogel was evaluated on the wounds of diabetic mice (Fig. 6a). The blood glucose level of KM mice was measured on the 14th day after STZ injection. Mice with blood glucose >16.7 mmol/L and body weight loss were considered diabetic mice (Figs. 6b1 and 6b2) [56]. The photothermal effect of the NIR-irradiated $PBON_2$ hydrogel in vivo was examined as well (Fig. 6c). The temperature of $PBON_2$ hydrogel was 19.2 °C (50.7 °C) without (with) NIR irradiation, which was sufficient to achieve photothermal inhibition. A round full-thickness skin wound of 8-mm diameter was created near the active hip of diabetic mice (an area that undergoes stretching, twisting, and compression), which was infected with *S. aureus* for 2 h. Afterward, the wounds were treated with PBO, $PBON_2$, or $PBON_2$ hydrogel with NIR irradiation ($PBON_2$+NIR). On Days 0, 3, 7, 14, and 21, the wound size was recorded and the tissue was excised to evaluate wound healing [57].

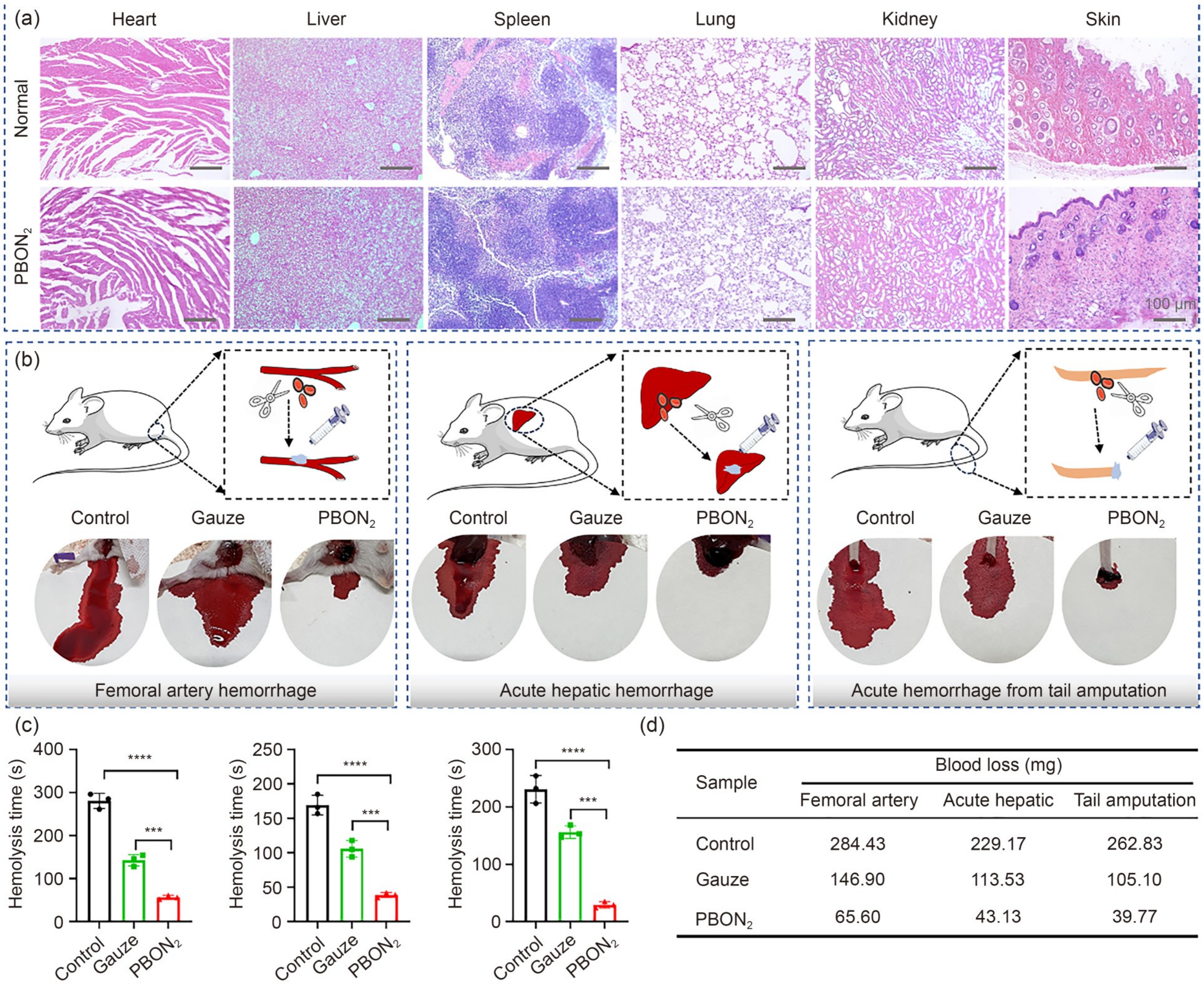

Sample	Blood loss (mg)		
	Femoral artery	Acute hepatic	Tail amputation
Control	284.43	229.17	262.83
Gauze	146.90	113.53	105.10
$PBON_2$	65.60	43.13	39.77

Fig. 5 Biocompatibility and hemostasis of $PBON_2$ hydrogel in vivo. (a) H&E staining of major organs, hypodermis, and skin of $PBON_2$ hydrogel-implanted and normal mice. (b) Schematic diagrams and photographs of femoral artery hemorrhage, acute hepatic hemorrhage, and acute tail hemorrhage. (c) Statistical analysis of hemolysis time for femoral artery hemorrhage, acute hepatic hemorrhage, and acute tail hemorrhage. (d) Statistical analysis of blood loss for femoral artery hemorrhage, acute hepatic hemorrhage, and acute tail hemorrhage. Data are expressed as mean±standard deviation (n=3); $^{***}p<0.001$, $^{****}p<0.0001$

Macroscopically, wound healing of the three hydrogel-treated groups (PBO, $PBON_2$, $PBON_2$+NIR) was faster than that in the control group (Figs. 6d1 and 62). Interestingly, a larger wound area was still visible in the control group at Days 7 and 21, with 37.74% and 65.48% healing rates, respectively (Fig. 6e). In contrast, the fastest wound closure and highest healing rate were observed in the $PBON_2$+NIR group, at 63.62% (Day 7) and 90.27% (Day 21), respectively. These results suggest that $PBON_2$ hydrogel combined with NIR treatment significantly improved wound healing.

3.9 Evaluation of wound healing: antibacterial effect, oxidative stress, and histological staining

Given the good antioxidant and antimicrobial abilities of PBON hydrogels in vitro, we collected wound tissues on Day 3 to analyze whether these bioactive hydrogels could eliminate infection in vivo [58]. The bactericidal rates in the PBO and $PBON_2$ groups were 44.16% and 56.05%, respectively, compared to the control group (Figs. 7a1 and 7a2), while that in the $PBON_2$+NIR group was close to 100%. This indicates that $PBON_2$+NIR has highly effective antibacterial activity at the wound site and that the inherent bacteriostatic property of $PBON_2$ hydrogel provides a long-term antimicrobial effect.

In addition, histochemical analysis was performed to assess ROS levels after treatment. The ROS level was measured at the early stage of wound healing by Dihydroethidium (DHE) staining on Day 3. Many fluorescent signals were observed in the control group (Fig. 7b1), indicating a high level of oxidative stress at the wound site. In contrast, the PBO and $PBON_2$ groups showed weaker fluorescence signals, and the $PBON_2$+NIR group had the weakest fluorescence

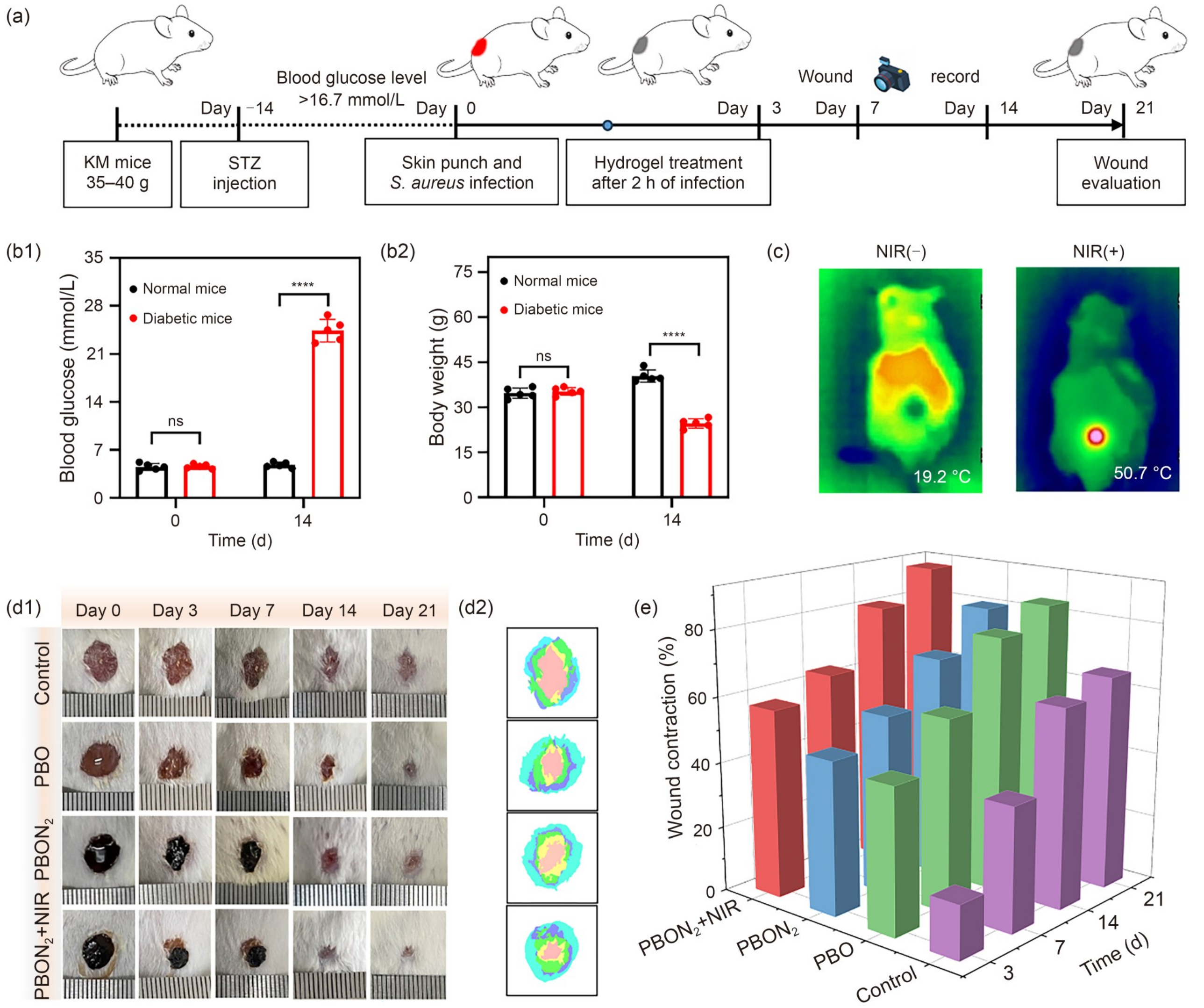

Fig. 6 Establishment and treatment of the *S. aureus*-infected diabetic wound model. (a) Schematic diagram of STZ-induced diabetic mice, modeling of infected wounds, and hydrogel treatment. (b) Blood glucose monitoring and body weight changes. (c) Thermal images of PBON$_2$ hydrogel with and without NIR irradiation. (d) Photographs of wound healing on Days 0, 3, 7, 14, and 21 and tracing graphs of wound healing. (e) Statistical 3D histograms of wound healing rates in control, PBO, PBON$_2$, and PBON$_2$+NIR groups. Data are expressed as mean±standard deviation ($n \geqslant 3$); $^{****}p<0.0001$; ns: not significant

signal. The quantitative analysis of fluorescence staining is shown in Fig. 7b2; the ROS content of the PBON$_2$+NIR group was significantly lower than that of the control group ($p<0.0001$), PBO group ($p<0.001$), and PBON$_2$ group ($p<0.01$). This demonstrated that PBON$_2$+NIR treatment has an optimal effect on ROS removal and significantly decreases the level of oxidative stress at the wound site.

On Day 21 after treatment, the wound and nearby skin tissue were excised for histochemical analysis. The quality of the regenerated skin was evaluated using H&E and Masson staining [59]; this analysis provided further insights into the effect of the hydrogel on wound healing. A shortening of the dermal space of 4075, 3261, 3097, and 2119 μm, respectively, was observed (Fig. 7c). In addition, a clear inflammatory infiltrate was visible in the control group (Fig. 7e), indicating a severe inflammatory response at the site. In contrast, all hydrogel groups showed intact neoepidermis with tight connections to the underlying granulation tissue, suggesting that wound healing had entered the remodeling stage. Quantitative data confirmed an increase in epidermal thickness (Fig. 7f), whereas loose connections between the neoepidermis and the tissue underneath were observed in the control group. In addition, more hair follicles appeared in all hydrogel groups, especially in the PBON$_2$+NIR group, compared to the control group (Fig. 7g).

Masson staining results are shown in Fig. 7d. In the control group, wounds showed an accumulation of myofibrils and fibrils, with a relatively low interstitial collagen content (Fig. 7h), while collagen fibrils were haphazardly arranged in PBO and PBON$_2$ groups. In the PBON$_2$+NIR group, there

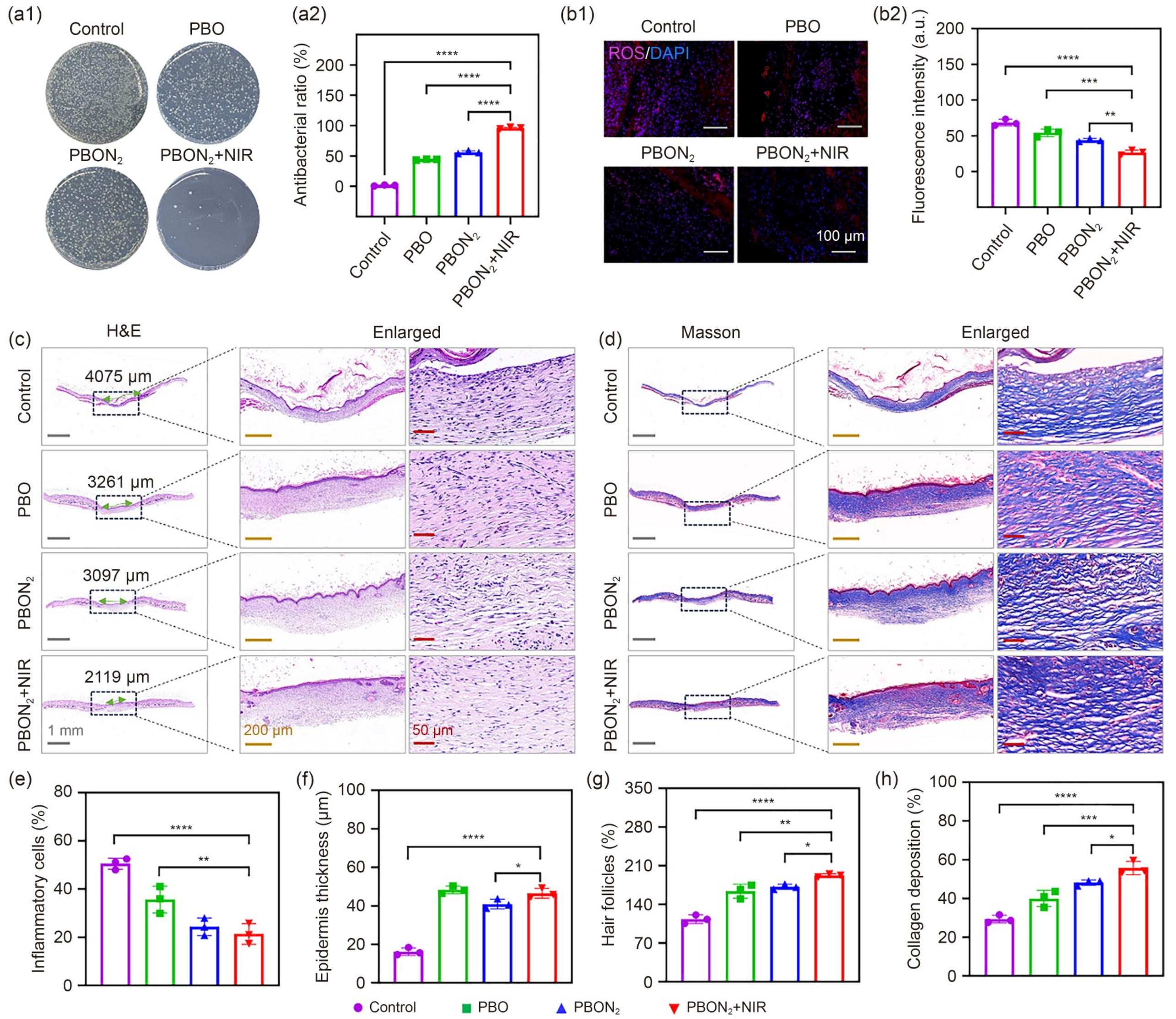

Fig. 7 Photothermal effect on oxidative stress in vivo, and H&E and Masson staining of healing tissues in each group. (a) Photographs of agar plate colonies of *S. aureus*-infected wounds and histograms of the antibacterial ratio in each group on Day 3. (b) Fluorescence staining of DHE and histograms of fluorescence intensity in each group on Day 3. (c) H&E staining images on Day 21 (green arrows indicate the dermal space). (d) Masson staining images on Day 21. (e) Histogram of the inflammatory cells. (f) Histogram of epidermal thickness. (g) Histogram of hair follicles. (h) Histogram of collagen deposition. Data are expressed as mean±standard deviation (n=3); $^{*}p<0.05$, $^{**}p<0.01$, $^{***}p<0.001$, $^{****}p<0.0001$

was a higher collagen deposition. Further, the PBON2+NIR-treated wounds showed the tightest and most homogeneous distribution of collagen fibers, indicating a significant improvement in ECM and tissue remodeling. It can be concluded that PBON2+NIR can promote collagen deposition, correct the abnormal state of deposited collagen fibers, and accelerate tissue regeneration in diabetic skin wounds.

3.10 Inflammation, angiogenesis, and cell proliferation

A disturbed and prolonged inflammatory response in chronic diabetic wounds leads to impaired fibroblast function, oxidative stress, impaired angiogenesis, and epithelial migration, ultimately leading to delayed wound healing [56]. Overexpression of the pro-inflammatory factors CD86, TNF-α, and IL-6 and underexpression of the anti-inflammatory factors CD206, IL-4, and IL-10 in diabetic wounds can be used as an indicator to assess the inflammatory response in diabetic wounds [49, 60, 61]. Immunofluorescence images (Fig. 8a) and quantitative analysis (Fig. 8b) showed that among all groups, the PBON2+NIR group had the lowest CD86, TNF-α, and IL-6 expression level ($p<0.0001$) and the highest expression level of CD206 ($p<0.001$), IL-4 ($p<0.0001$), and IL-10 ($p<0.0001$). Thus, PBON2+NIR treatment significantly reduced the inflammatory response in diabetic wounds.

Angiogenesis has a positive effect on the healing of chronic diabetic wounds and even the functional reconstruction of

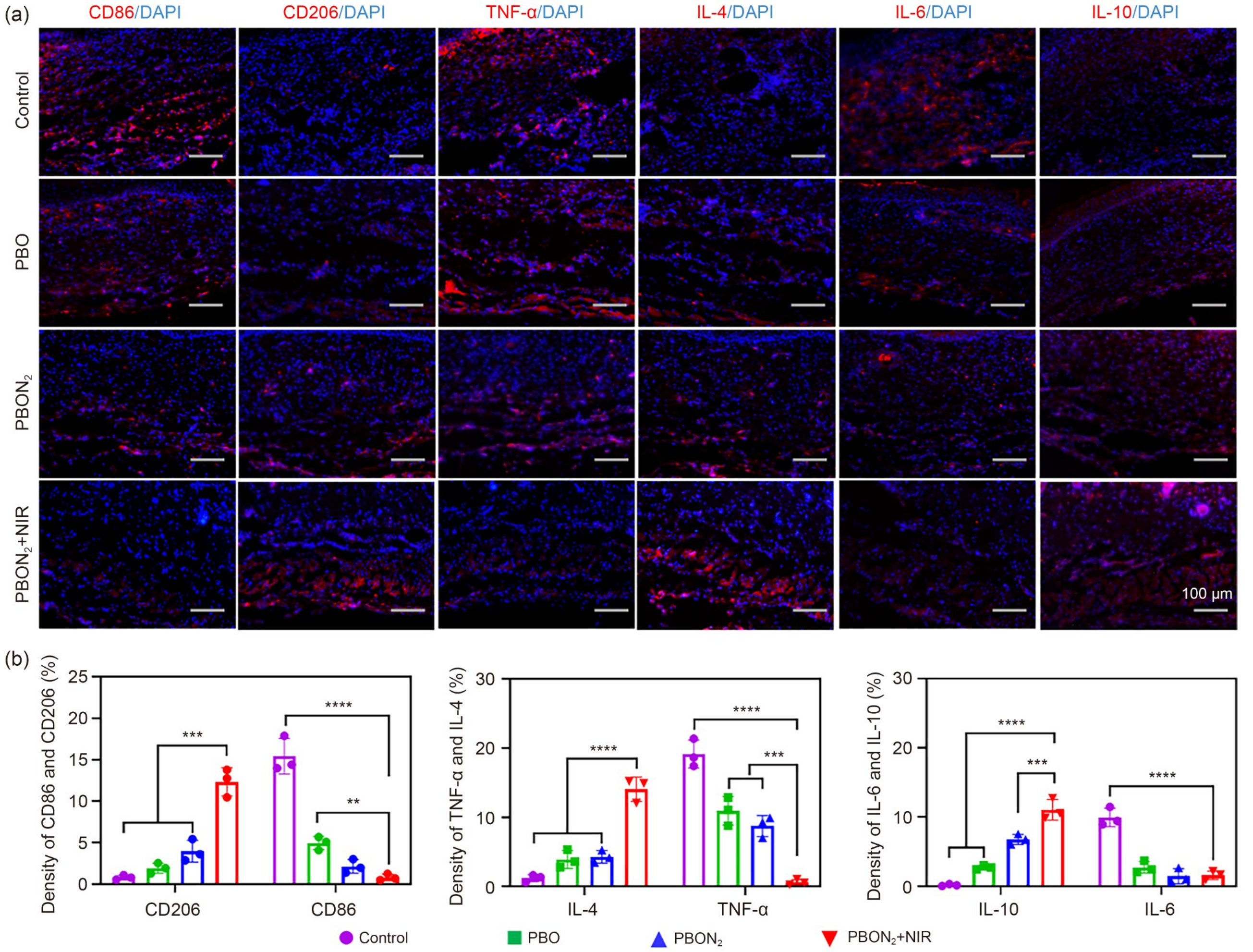

Fig. 8 Immunofluorescence images of inflammatory factors in wounds. (a) Fluorescence images of positive CD86, CD206, TNF-α, IL-4, IL-6, and IL-10 expression on Day 21. (b) Histograms of positive expression of inflammatory factors. Data are expressed as mean±standard deviation (n=3); $^{**}p$<0.01, $^{***}p$<0.001, $^{****}p$<0.0001

the skin [62]. Immunofluorescence labeling techniques for CD31, VEGF, and α-SMA are commonly used to analyze wound angiogenesis [63]. All hydrogel groups showed more neovascularization than the control group (Fig. 9a1). Further, the neovascularization was larger and densely distributed in the PBON$_2$+NIR group. Quantitative analysis showed that PBON$_2$+NIR significantly increased the expression of CD31, VEGF, and α-SMA at the wound bed (Fig. 9a2), showing the formation of additional capillaries and mature blood vessels through neovascularization.

PCNA is an important indicator of cell proliferation [64]. Immunofluorescence images of PCNA in each group are shown in Fig. 9b1, with the control group exhibiting the lowest fluorescence signal. In addition, the fluorescence signal of PCNA was highly enriched in the PBON$_2$+NIR group compared with the PBO and PBON$_2$ groups. Our quantitative analysis confirmed that the hydrogel treatment effectively promotes cell proliferation, with the PBON$_2$+NIR treatment being optimal (Fig. 9b2).

4 Conclusions

In summary, a rapid gelation hydrogel PBON with multiple functionalities based on PVA, Borax, OPC, and AuPt@PDA nanozymes was developed by mixing. The dual enzymatic activities (GO$_x$-like and CAT-like) derived from the nanozymes can produce O$_2$ while reducing glucose concentration and depleting H$_2$O$_2$ through a cascade reaction, which may counteract the adverse microenvironment (high glucose, high ROS, and hypoxia) in diabetic wounds. For a nanozyme concentration of 1 mg/mL, the photothermal conversion efficiency of PBON$_2$ reached 81.9%. The temperature of PBON$_2$ rapidly increased to 49.7 °C and was able to kill bacteria under 808-nm NIR with an optical density of 0.3 W/cm^2, which is lower than the maximum safe allowable limit. Furthermore, PBON$_2$ possesses strong tissue-adhesion and deformability properties to match the dynamic demands in highly mobile regions. In vivo analysis of skin wounds showed that a multifunctional PBON$_2$ hydrogel dressing

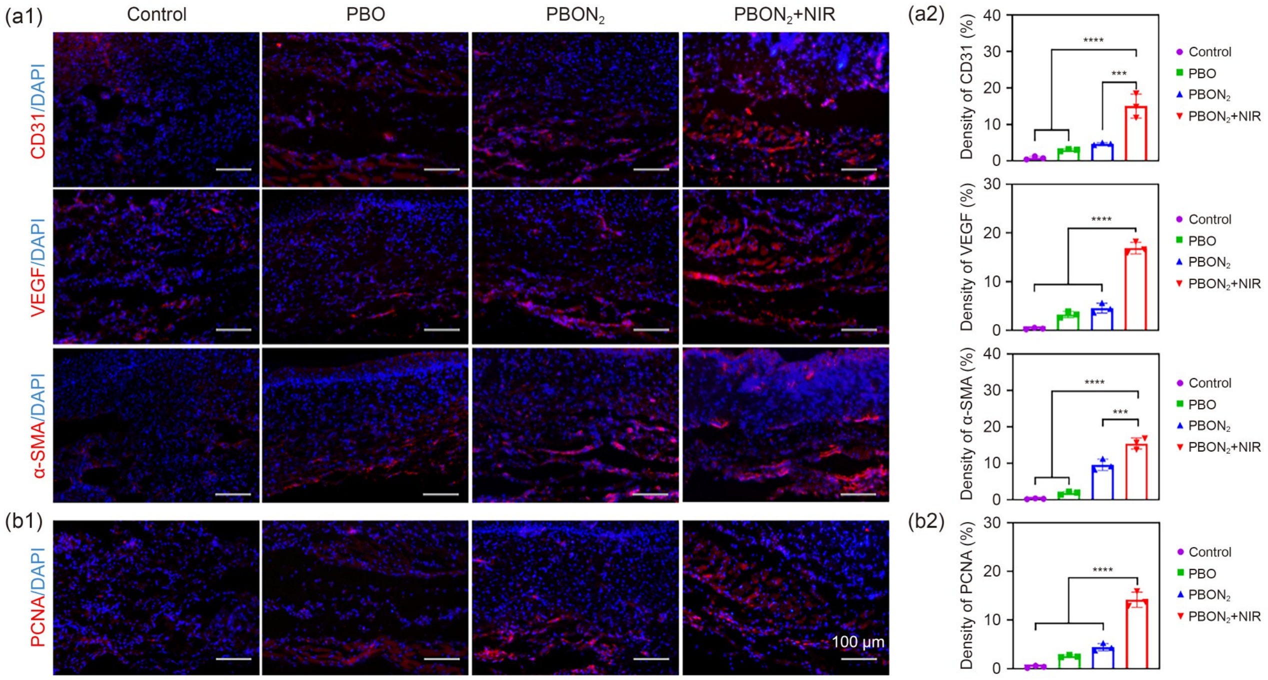

Fig. 9 Immunofluorescence images of vascular regeneration in damaged wounds. (a) Fluorescence images and associated histograms of CD31, VEGF, and α-SMA expression on Day 21. (b) Fluorescence images and associated histograms of PCNA expression on Day 21. Data are expressed as mean±standard deviation (n=3); $^{***}p<0.001$, $^{****}P<0.0001$

loaded with nanozymes significantly promoted the healing of diabetic wounds in highly mobile regions by disrupting hyperglycemia-induced bacterial infection and elevated ROS levels, alleviating the inflammatory response, promoting epidermal regeneration and collagen deposition, and accelerating angiogenesis. Therefore, this approach could be an ideal therapeutic strategy for the treatment of skin wounds in highly mobile regions of diabetic patients.

Supplementary Information The online version contains supplementary material available at https://doi.org/10.1631/bdm.2400375.

Acknowledgements This work was financially supported by the National Natural Science Foundation of China (No. U1804198) to MHY, Zhongyuan Thousand Talents Project (No. 204200510013) to FXG, and Key Scientific and Technological Research Projects in Henan Province (No. 232102311098) to RMJ. We also thank the Center for Modern Analysis and Gene Sequencing, Zhengzhou University, for the facility support.

Author contributions KYL: resources, writing—original draft, and preparation. RMJ: investigation and writing—review & editing. MYY: methodology and preparation. YCY: methodology and preparation. JML: methodology and preparation. CHL: methodology. CZ: methodology. HZ: methodology. DHZ: conceptualization, validation, and writing—review & editing. FXG: conceptualization, writing—review & editing. MHY: conceptualization, validation, investigation, and writing—review & editing.

Declarations

Conflict of interest The authors declare that they have no conflict of interest.

Ethical approval All the animal use protocols were approved by the Zhengzhou University Animal Ethics and Protection Committee (approval number: ZZUIRB2023-138).

Data availability The data that support the findings of this study are available from the corresponding authors upon reasonable request.

References

1. Zhang Z, Huang CL, Guan SY et al (2024) Hybrid gelatin-ascorbyl phosphate scaffolds accelerate diabetic wound healing via ROS scavenging, angiogenesis and collagen remodeling. Biomater Adv 158:213779. https://doi.org/10.1016/j.bioadv.2024.213779
2. Zhou ZP, Deng T, Tao MX et al (2023) Snail-inspired AFG/GelMA hydrogel accelerates diabetic wound healing via inflammatory cytokines suppression and macrophage polarization. Biomaterials 299:122141. https://doi.org/10.1016/j.biomaterials.2023.122141
3. Yang ZF, Huang RK, Zheng BN et al (2021) Highly stretchable, adhesive, biocompatible, and antibacterial hydrogel dressings for wound healing. Adv Sci 8(8):2003627. https://doi.org/10.1002/advs.202003627
4. Xin PK, Han SY, Huang J et al (2023) Natural okra-based hydrogel for chronic diabetic wound healing. Chin Chem Lett 34(8):108125. https://doi.org/10.1016/j.cclet.2022.108125
5. Pruett LJ, Jenkins CH, Singh NS et al (2021) Heparin microislands in microporous annealed particle scaffolds for accelerated diabetic wound healing. Adv Funct Mater 31(35):2104337. https://doi.org/10.1002/adfm.202104337
6. Lei LJ, Zhu YL, Qin XY et al (2021) Magnetic biohybrid microspheres for protein purification and chronic wound healing in diabetic mice. Chem Eng J 425:130671. https://doi.org/10.1016/j.cej.2021.130671

7. Pan WH, Qi XL, Xiang YJ et al (2022) Facile formation of injectable quaternized chitosan/tannic acid hydrogels with antibacterial and ROS scavenging capabilities for diabetic wound healing. Int J Biol Macromol 195:190–197. https://doi.org/10.1016/j.ijbiomac.2021.12.007
8. Ma HS, Zhou Q, Chang J et al (2019) Grape seed-inspired smart hydrogel scaffolds for melanoma therapy and wound healing. ACS Nano 13(4):4302–4311. https://doi.org/10.1021/acsnano.8b09496
9. Zhu SL, Zhao BJ, Li MC et al (2023) Microenvironment responsive nanocomposite hydrogel with NIR photothermal therapy, vascularization and anti-inflammation for diabetic infected wound healing. Bioact Mater 26:306–320. https://doi.org/10.1016/j.bioactmat.2023.03.005
10. Yu YL, Li PF, Zhu CL et al (2019) Multifunctional and recyclable photothermally responsive cryogels as efficient platforms for wound healing. Adv Funct Mater 29(35):1904402. https://doi.org/10.1002/adfm.201904402
11. Yang Y, Ma L, Cheng C et al (2018) Nonchemotherapic and robust dual-responsive nanoagents with on-demand bacterial trapping, ablation, and release for efficient wound disinfection. Adv Funct Mater 28(21):1705708. https://doi.org/10.1002/adfm.201705708
12. Guo ZY, Zhang ZZ, Zhang N et al (2022) A Mg^{2+}/polydopamine composite hydrogel for the acceleration of infected wound healing. Bioact Mater 15:203–213. https://doi.org/10.1016/j.bioactmat.2021.11.036
13. Maleki A, He J, Bochani S et al (2021) Multifunctional photoactive hydrogels for wound healing acceleration. ACS Nano 15(12): 18895–18930. https://doi.org/10.1021/acsnano.1c08334
14. He LN, Di DH, Chu XH et al (2023) Photothermal antibacterial materials to promote wound healing. J Controlled Release 363: 180–200. https://doi.org/10.1016/j.jconrel.2023.09.035
15. Wen T, Yang AY, Wang T et al (2020) Ultra-small platinum nanoparticles on gold nanorods induced intracellular ROS fluctuation to drive megakaryocytic differentiation of leukemia cells. Biomater Sci 8(22):6204–6211. https://doi.org/10.1039/d0bm01547d
16. Liu W, Zhao NN, Yin Q et al (2023) Injectable hydrogels encapsulating dual-functional Au@Pt core–shell nanoparticles regulate infarcted microenvironments and enhance the therapeutic efficacy of stem cells through antioxidant and electrical integration. ACS Nano 17(3):2053–2066. https://doi.org/10.1021/acsnano.2c07436
17. Zhang B, Lv YJ, Yu CG et al (2022) Au–Pt nanozyme-based multifunctional hydrogel dressing for diabetic wound healing. Biomater Adv 137:212869. https://doi.org/10.1016/j.bioadv.2022.212869
18. Lu BL, Lin FC, Jiang X et al (2017) One-pot assembly of microfibrillated cellulose reinforced PVA–borax hydrogels with self-healing and pH-responsive properties. ACS Sustain Chem Eng 5(1):948–956. https://doi.org/10.1021/acssuschemeng.6b02279
19. Cho SW, Hwang SY, Oh DX et al (2021) Recent progress in self-healing polymers and hydrogels based on reversible dynamic B–O bonds: boronic/boronate esters, borax, and benzoxaborole. J Mater Chem A 9(26):14630–14655. https://doi.org/10.1039/D1TA02308J
20. Wang HX, Biswas SK, Zhu SL et al (2020) Self-healable electroconductive hydrogels based on core-shell structured nanocellulose/carbon nanotubes hybrids for use as flexible supercapacitors. Nanomaterials 10(1):112. https://doi.org/10.3390/nano10010112
21. Zhu JY, Tsehaye MT, Wang J et al (2018) A rapid deposition of polydopamine coatings induced by iron (III) chloride/hydrogen peroxide for loose nanofiltration. J Colloid Interface Sci 523:86–97. https://doi.org/10.1016/j.jcis.2018.03.072
22. Guo LR, Panderi I, Yan DD et al (2013) A comparative study of hollow copper sulfide nanoparticles and hollow gold nanospheres on degradability and toxicity. ACS Nano 7(10):8780–8793. https://doi.org/10.1021/nn403202w
23. Ciou TY, Korupalli C, Chou TH et al (2021) Biomimetic nanoreactor for cancer eradication via win–win cooperation between starvation/photo/chemodynamic therapies. ACS Appl Bio Mater 4(7):5650–5660. https://doi.org/10.1021/acsabm.1c00452
24. Liu KY, Zhao DH, Zhao H et al (2024) Mild hyperthermia-assisted chitosan hydrogel with photothermal antibacterial property and CAT-like activity for infected wound healing. Int J Biol Macromol 254:128027. https://doi.org/10.1016/j.ijbiomac.2023.128027
25. Zeng QK, Qian YN, Huang YJ et al (2021) Polydopamine nanoparticle-dotted food gum hydrogel with excellent antibacterial activity and rapid shape adaptability for accelerated bacteria-infected wound healing. Bioact Mater 6(9):2647–2657. https://doi.org/10.1016/j.bioactmat.2021.01.035
26. Lin XL, Fu T, Lei YQ et al (2023) An injectable and light curable hyaluronic acid composite gel with anti-biofilm, anti-inflammatory and pro-healing characteristics for accelerating infected wound healing. Int J Biol Macromol 253:127190. https://doi.org/10.1016/j.ijbiomac.2023.127190
27. Fan PH, Dong Q, Yang JF et al (2023) Flexible dual-functionalized hyaluronic acid hydrogel adhesives formed in situ for rapid hemostasis. Carbohydrate Polymers 313:120854. https://doi.org/10.1016/j.carbpol.2023.120854
28. Yao KT, Li SY, Zheng XZ et al (2024) Superwettable calcium ion exchanged carboxymethyl cellulose powder with self-gelation, tissue adhesion and bioabsorption for effective hemorrhage control. Chem Eng J 481:148770. https://doi.org/10.1016/j.cej.2024.148770
29. Bao XF, Zhao JH, Sun J et al (2018) Polydopamine nanoparticles as efficient scavengers for reactive oxygen species in periodontal disease. ACS Nano 12(9):8882–8892. https://doi.org/10.1021/acsnano.8b04022
30. Xiang T, Guo QR, Jia LH et al (2024) Multifunctional hydrogels for the healing of diabetic wounds. Adv Healthc Mater 13(1): 2301885. https://doi.org/10.1002/adhm.202301885
31. Huang CL, Zhang Z, Fang YF et al (2024) Cost-effective and natural-inspired lotus root/GelMA scaffolds enhanced wound healing via ROS scavenging, angiogenesis and reepithelialization. Int J Biol Macromol 278:134496. https://doi.org/10.1016/j.ijbiomac.2024.134496
32. He JH, Zhang ZX, Yang YT et al (2021) Injectable self-healing adhesive pH-responsive hydrogels accelerate gastric hemostasis and wound healing. Nano-Micro Lett 13(1):80. https://doi.org/10.1007/s40820-020-00585-0
33. Gan DL, Shuai T, Wang X et al (2020) Mussel-inspired redox-active and hydrophilic conductive polymer nanoparticles for adhesive hydrogel bioelectronics. Nano-Micro Lett 12(1):169. https://doi.org/10.1007/s40820-020-00507-0
34. Yi XT, He JM, Wei XJ et al (2023) A polyphenol and ε-polylysine functionalized bacterial cellulose/PVA multifunctional hydrogel for wound healing. Int J Biol Macromol 247:125663. https://doi.org/10.1016/j.ijbiomac.2023.125663
35. Qu J, Zhao X, Liang YP et al (2018) Antibacterial adhesive injectable hydrogels with rapid self-healing, extensibility and compressibility as wound dressing for joints skin wound healing. Biomaterials 183:185–199. https://doi.org/10.1016/j.biomaterials.2018.08.044
36. Qi XL, Cai EY, Xiang YJ et al (2023) An immunomodulatory hydrogel by hyperthermia-assisted self-cascade glucose depletion

and ROS scavenging for diabetic foot ulcer wound therapeutics. Adv Mater 35(48):2306632. https://doi.org/10.1002/adma.202306632
37. Kim SK, Lee GH, Jeon C et al (2022) Bimetallic nanocatalysts immobilized in nanoporous hydrogels for long-term robust continuous glucose monitoring of smart contact lens. Adv Mater 34(18):2110536. https://doi.org/10.1002/adma.202110536
38. Yang ZX, Ren KX, Chen YH et al (2024) Oxygen-generating hydrogels as oxygenation therapy for accelerated chronic wound healing. Adv Healthc Mater 13(3):2302391. https://doi.org/10.1002/adhm.202302391
39. Huang XS, Liang BM, Zheng ST et al (2024) Microarrow sensor array with enhanced skin adhesion for transdermal continuous monitoring of glucose and reactive oxygen species. Bio-Des Manuf 7(1):14–30. https://doi.org/10.1007/s42242-023-00246-2
40. Chen F, Song T (2022) AuPt bimetallic nanozymes for enhanced glucose catalytic oxidase. Front Chem 10:854516. https://doi.org/10.3389/fchem.2022.854516
41. Cheng S, Pan M, Hu DR et al (2023) Adhesive chitosan-based hydrogel assisted with photothermal antibacterial property to prompt mice infected skin wound healing. Chin Chem Lett 34(12): 108276. https://doi.org/10.1016/j.cclet.2023.108276
42. Baliyan S, Mukherjee R, Priyadarshini A et al (2022) Determination of antioxidants by DPPH radical scavenging activity and quantitative phytochemical analysis of *Ficus* religiosa. Molecules 27(4):1326. https://doi.org/10.3390/molecules27041326
43. Song WQ, Xu TT, Qian LW et al (2023) Eco-friendly cellulose-based hydrogel functionalized by NIR-responsive multimodal antibacterial polymeric ionic liquid as platform for promoting wound healing. Int J Biol Macromol 244:125353. https://doi.org/10.1016/j.ijbiomac.2023.125353
44. Xu K, Deng SJ, Zhu YB et al (2023) Platelet rich plasma loaded multifunctional hydrogel accelerates diabetic wound healing via regulating the continuously abnormal microenvironments. Adv Healthc Mater 12(28):2301370. https://doi.org/10.1002/adhm.202301370
45. Liang YQ, Li ZL, Huang Y et al (2021) Dual-dynamic-bond cross-linked antibacterial adhesive hydrogel sealants with on-demand removability for post-wound-closure and infected wound healing. ACS Nano 15(4):7078–7093. https://doi.org/10.1021/acsnano.1c00204
46. He XJ, Dai LX, Ye LS et al (2022) A vehicle-free antimicrobial polymer hybrid gold nanoparticle as synergistically therapeutic platforms for *Staphylococcus aureus* infected wound healing. Adv Sci 9(14):2105223. https://doi.org/10.1002/advs.202105223
47. Zhang SN, Lu QJ, Wang FY et al (2021) Gold–platinum nanodots with high-peroxidase-like activity and photothermal conversion efficiency for antibacterial therapy. ACS Appl Mater Interfaces 13(31):37535–37544. https://doi.org/10.1021/acsami.1c10600
48. Tao BL, Lin CC, Yuan Z et al (2021) Near infrared light-triggered on-demand Cur release from Gel-PDA@Cur composite hydrogel for antibacterial wound healing. Chem Eng J 403:126182. https://doi.org/10.1016/j.cej.2020.126182
49. Xu HT, Li YQ, Song JP et al (2024) Highly active probiotic hydrogels matrixed on bacterial EPS accelerate wound healing via maintaining stable skin microbiota and reducing inflammation. Bioact Mater 35:31–44. https://doi.org/10.1016/j.bioactmat.2024.01.011
50. Guo CA, Zhang J, Feng XJ et al (2022) Polyhexamethylene biguanide chemically modified cotton with desirable hemostatic, inflammation-reducing, intrinsic antibacterial property for infected wound healing. Chin Chem Lett 33(6):2975–2981. https://doi.org/10.1016/j.cclet.2021.12.086
51. Zhao XQ, Shi YC, Niu SF et al (2024) Enhancing wound healing and bactericidal efficacy: a hydrogel membrane of bacterial cellulose and sanxan gel for accelerating the healing of infected wounds. Adv Healthc Mater 13(8):2303216. https://doi.org/10.1002/adhm.202303216
52. He YM, Liu KY, Zhang C et al (2022) Facile preparation of PVA hydrogels with adhesive, self-healing, antimicrobial, and on-demand removable capabilities for rapid hemostasis. Biomater Sci 10(19):5620–5633. https://doi.org/10.1039/d2bm00891b
53. Rajakumari R, Volova T, Oluwafemi OS et al (2020) Nano formulated proanthocyanidins as an effective wound healing component. Mater Sci Eng C 106:110056. https://doi.org/10.1016/j.msec.2019.110056
54. Osman A, Lin EH, Hwang DS (2023) A sticky carbohydrate meets a mussel adhesive: catechol-conjugated levan for hemostatic and wound healing applications. Carbohydrate Polymers 299:120172. https://doi.org/10.1016/j.carbpol.2022.120172
55. Liu KY, Zhang C, Chang R et al (2023) Ultra-stretchable, tissue-adhesive, shape-adaptive, self-healing, on-demand removable hydrogel dressings with multiple functions for infected wound healing in regions of high mobility. Acta Biomater 166:224–240. https://doi.org/10.1016/j.actbio.2023.05.025
56. Tan WW, Long T, Wan YZ et al (2023) Dual-drug loaded polysaccharide-based self-healing hydrogels with multifunctionality for promoting diabetic wound healing. Carbohydrate Polymers 312:120824. https://doi.org/10.1016/j.carbpol.2023.120824
57. Qian YN, Zheng YJ, Jin J et al (2022) Immunoregulation in diabetic wound repair with a photoenhanced glycyrrhizic acid hydrogel scaffold. Adv Mater 34(29):2200521. https://doi.org/10.1002/adma.202200521
58. Zhang KB, Yang C, Cheng CX et al (2022) Bioactive injectable hydrogel dressings for bacteria-infected diabetic wound healing: a “pull–push” approach. ACS Appl Mater Interfaces 14(23): 26404–26417. https://doi.org/10.1021/acsami.2c04300
59. Zhao XD, Pei DD, Yang YX et al (2021) Green tea derivative driven smart hydrogels with desired functions for chronic diabetic wound treatment. Adv Funct Mater 31(18):2009442. https://doi.org/10.1002/adfm.202009442
60. Liu J, Qu MY, Wang CR et al (2022) A dual-cross-linked hydrogel patch for promoting diabetic wound healing. Small 18(17): 2106172. https://doi.org/10.1002/smll.202106172
61. Navarro-González JF, Mora-Fernández C (2008) The role of inflammatory cytokines in diabetic nephropathy. J Am Soc Nephrol 19(3): 433–442. https://doi.org/10.1681/ASN.2007091048
62. Matoori S, Veves A, Mooney DJ (2021) Advanced bandages for diabetic wound healing. Sci Transl Med 13(585):eabe4839. https://doi.org/10.1126/scitranslmed.abe4839
63. Jiang T, Liu SJ, Wu ZH et al (2022) ADSC-exo@MMP-PEG smart hydrogel promotes diabetic wound healing by optimizing cellular functions and relieving oxidative stress. Mater Today Bio 16:100365. https://doi.org/10.1016/j.mtbio.2022.100365
64. Ren Y, Aierken A, Zhao L et al (2022) hUC-MSCs lyophilized powder loaded polysaccharide ulvan driven functional hydrogel for chronic diabetic wound healing. Carbohydrate Polymers 288: 119404. https://doi.org/10.1016/j.carbpol.2022.119404